communications earth & environment

ARTICLE

https://doi.org/10.1038/s43247-021-00250-3 OPEN

Preconditioning, aerosols, and radiation control the temperature of glaciation in Amazonian clouds

Alexandre L. Correia [1✉], Elisa T. Sena[2], Maria A. F. Silva Dias[3] & Ilan Koren [4]

Glaciation in clouds is a fundamental phenomenon in determining Earth's radiation fluxes, sensible and latent heat budgets in the atmosphere, the water cycle, cloud development and lifetime. Nevertheless, the main mechanisms that govern the temperature of glaciation in clouds have not been fully identified. Here we present an analysis of 15 years (2000-2014) of satellite, sunphotometer, and reanalysis datasets over the Amazon. We find that the temperature of glaciation in convective clouds is controlled by preconditioning dynamics, natural and anthropic aerosols, and radiation. In a moist atmospheric column, prone to deep convection, increasing the amount of aerosols leads to a delay in the onset of glaciation, reducing the glaciation temperature. For a dry column, radiative extinction by biomass burning smoke leads to atmospheric stabilization and an increase in the glaciation temperature. Our results offer observational benchmarks that can help a more precise description of glaciation in convective cloud models.

[1] Institute of Physics, University of São Paulo, São Paulo, Brazil. [2] Multidisciplinary Department, Federal University of São Paulo, Osasco, Brazil. [3] Instituto de Astronomia, Geofísica e Ciências Atmosféricas, Universidade de São Paulo, São Paulo, Brazil. [4] Weizmann Institute of Science, Rehovot, Israel. ✉email: acorreia@if.usp.br

Microphysical interactions between aerosol particles and cloud droplets can lead to a delay in total glaciation in deep convective clouds[1], according to results from modeling and observational[2] studies. Cloud development and lifetime, and their response to radiation and aerosols remain some of the most important issues that need to be improved in climate modeling[3–5]. Glaciation is a fundamental ingredient controlling cloud lifetime and precipitation[6], hence understanding further how it can be influenced by aerosols, radiation, and dynamics constitutes an important piece of this puzzle.

The temperature of total glaciation[7] (T_g^*) can be defined as the warmest section of the glaciated phase in clouds, considering the accuracy and spatial resolution of the instrumentation in use[8]. T_g^* can be anywhere between a few degrees below 0 °C and −38 °C[9], and it is regulated by complex in-cloud physical processes. For instance, the magnitude of updraft speed in a mixed-phase section of a convective cloud can modulate the local vapor supersaturation, which controls whether droplets and/or ice particles can grow[8], depending on the number concentration and size distribution of water droplets and ice particles[8]. These glaciation-controlling interactions between cloud microphysics and dynamics cannot be fully represented in global climate models[5]. Even though T_g^* is critical to define the mixed-phase cloud section in equilibrium climate sensitivity studies[4,5], we have limited observational knowledge of this variable, and it remains to be determined whether it could be used to circumscribe climate modeling scenarios.

Here we distinguish T_g^* (i.e., a temperature that can be measured in situ) from T_g, a proxy estimate of T_g^*, derived from indirect measurements. Although past studies have observed how properties, such as cloud top temperature, respond to dynamics and aerosols in the atmosphere[10], there have been few in situ measurements of T_g^* itself[11–15]. Some observational analyses, from space or ground-based remote sensing, have shown how T_g can be retrieved for single maritime or continental clouds[7,11,16,17], or how T_g can correlate with aerosols from dust and forest fire events[18]. Notice all these previous estimates of T_g^* correspond to particular case studies, not accounting for long-term meteorological variability or site-specific aerosol properties[16,18]. We still lack robust statistics based on basic observational evidence to understand how dynamical forcing, radiation, and aerosols influence T_g^*, particularly in deep tropical clouds. For instance, deep convective clouds in the Amazon are periodically subjected to heavily polluted atmospheric conditions that occur yearly, from August to October, due to the prevalent use of fire as a land-clearing tool[19]. This situation induces micro- and macrophysical changes that have been observed in Amazonian clouds[20–22] but the effect of biomass burning smoke on T_g^*, coupled with other drivers of cloud dynamics, remains uncertain.

The challenge here is to understand the relative role of key players that control T_g^* in the Amazon. The association of intense solar heating and abundant humidity[23,24] with weak vertical wind shear[2,25] in this region leads to frequent atmospheric instability. Large scale convergence and mesoscale organization[26] modulate the vertical transport of moisture[27]. Dynamics determine the local atmospheric humidity profile that defines a fundamental feedback pathway for the preconditioning effect and the development of deep convection[27–29]. When a parcel ascends through a moist column, a smaller humidity gradient implies that less of its buoyant energy is eroded by the surrounding drier environment, favoring the development of deeper convection cells[27,29]. Strong updrafts can push the total glaciation level upward[11,30], decreasing T_g^* and driving deep convection up to the upper troposphere[31], where changes in lapse rate and vertical pressure gradient cause cloud detrainment. This contributes to humidifying the vicinity of cloud tops[32], preconditioning the surrounding environmental air to the formation and growth of other convective cells[28]. From the microphysical point of view, aerosols can decrease T_g^* by delaying droplet freezing[17,20]. In the warm phase, aerosols acting as cloud condensation nuclei reduce droplet effective radii, and the efficiency of collision-coalescence processes, in favor of diffusional growth. Increased vapor diffusion boosts the release of latent heat of condensation, which in turn leads to increased buoyancy and updrafts. As a consequence, more droplets, with smaller average sizes, are taken aloft to temperatures below the 0 °C isotherm[33]. These smaller supercooled droplets result in less efficient heterogeneous freezing, hence glaciation occurs higher in the atmosphere, at a lower T_g^*. The delayed freezing releases latent heat higher in the atmospheric column, which fuels buoyancy and strengthens updrafts, bringing more moisture from lower levels, and favors the formation of deeper clouds[2,34]. On the other hand, some types of aerosols can also act as ice-forming nuclei[35,36], inducing glaciation in clouds[36]. Lastly, under heavily polluted conditions the extinction of sunlight by the aerosol layer in cloud-free areas can change the vertical temperature profile and alter surface heat fluxes[22,37]. This in turn can curtail convection patterns locally[22], reduce updraft motion, and hence influence the development of deep convective clouds and the onset of glaciation[8].

Here we show how T_g in Amazonian deep convective clouds responds to the aerosol load in the atmosphere, depending on the preconditioned state of the upper troposphere. By combining 15 years of satellite, ground-based sunphotometer[38], and reanalysis data[39,40], we confirm the pivotal part humidity represents as a dynamical forcing controlling deep convection in the Amazon, and reveal the complexity of interactions between aerosol microphysics, radiative effects, and the humidification of the atmospheric column. The retrieved T_g patterns are consistent with direct measurements reported in previous studies, and with microphysical mechanisms affecting glaciation. T_g can also be controlled by the combined influence of dynamics and aerosol radiative effects originated from severe biomass burning pollution.

Results and discussion

We mark T_g as an estimator of T_g^*, derived from satellite data using a ratio between the reflectance at two wavelengths that are sensitive to the thermodynamic phase (*cf.* Methods). This allows for a good approximation for the temperature at which most of the hydrometeors are in the solid phase. Comparisons between T_g and in situ measurements are examined further ahead.

A proxy for the local dynamical forcing. In order to define a proxy for the dynamical forcing, one needs to find a set of meteorological variables that show the highest absolute correlation with T_g (R_{Tg} in Table 1), while being nearly independent of the microphysical forcing represented by the aerosol optical depth (τ_a) with the lowest absolute correlation ($R_{\tau a}$), a procedure that has been used in other studies[34]. A large number of meteorological and surface parameters in reanalysis datasets[39,40] (Supplementary Table 1) were investigated to that end, in four synoptic times from 0 to 18 UTC. The top results are shown in Table 1 (correlation p values all under 0.05).

The first three variables in Table 1 are specific and relative humidity at high levels in the troposphere, from 225 to 350 hPa, for which R_{Tg} varies from about −0.25 to −0.18, while $R_{\tau a}$ ranges between −0.03 and −0.04. The absolute values of R_{Tg} are expected to be small compared to unity, since it is probable different sources of random events may act during the long 15 y timeframe used in this study. The identification of humidity at high levels in association with the dynamical forcing is consistent

Table 1 Top correlations in the period 2000-2014, between ECMWF reanalysis variables and T_g (R_{Tg}), and between reanalysis variables and τ_a ($R_{\tau a}$).

Dataset[a]	Variable	Level	Correlation with T_g		Correlation with τ_a	
			R_{Tg}	p value	$R_{\tau a}$	p value
PL	Specific humidity	225 hPa	−0.2547	$<10^{-10}$	−0.0338	0.0030
PL	Relative humidity	300 hPa	−0.2274	$<10^{-10}$	−0.0315	0.0058
PL	Relative humidity	350 hPa	−0.1798	$<10^{-10}$	−0.0402	0.0004
SF	Clear sky photosynthetically active radiation	Surface	−0.1730	$<10^{-10}$	+0.0491	0.0001
PL	Cloud cover	150 hPa	−0.1525	$<10^{-10}$	−0.0305	0.0075
PL	Divergence	175 hPa	−0.1344	$<10^{-10}$	+0.0245	0.0318
PL	U component of wind	70 hPa	+0.1336	$<10^{-10}$	+0.0392	0.0006
PL	Cloud cover	250 hPa	−0.1330	$<10^{-10}$	−0.0350	0.0021
PL	Geopotential	825 hPa	+0.1202	$<10^{-10}$	+0.0330	0.0039
PL	U component of wind	125 hPa	+0.1192	$<10^{-10}$	+0.0335	0.0034

(a) ECMWF datasets used in the analyses: ERA-Interim Pressure Levels (PL), Era-Interim Surface[39] (SF), and Era-Interim/Land[40].

with a moistened (preconditioned) upper layer that favors convection and colder T_g (hence the negative correlation). The photosynthetically active radiation at the surface ($R_{Tg} = -0.17$) was also listed in Table 1, compatible with surface radiative warming in cloud-free areas generating atmospheric instability necessary for convective initiation. Also cloud cover at 150 hPa ($R_{Tg} = -0.15$) is consistent with an increased detrainment in the upper troposphere for conditions that favor deep convection. Humidity at lower to mid levels (1000-650 hPa) showed negligible or non-significant correlations with T_g and τ_a.

In principle, the reanalysis variables shown in Table 1 can be combined to define a proxy that represents the local dynamical forcing over T_g variability. We opted for simply considering the specific humidity at 225 hPa (q_{225}) as this index, which is used here just for segregating the data. More specifically, the tertiles in the distribution of q_{225} values were used to classify T_g and τ_a data in three subsets, corresponding to drier than average (D), average (A), and more moist than average (M) specific humidity classes in the upper troposphere, due to a varying degree of atmospheric preconditioning. Implicitly we are recognizing the upper tropospheric humidity as the most consequential dynamical parameter related to the development of deep convection in the Amazon, due to the moistening of the atmospheric column, as seen before[27–29] (*cf.* preconditioning analysis in SI). Other methodologies were tested to build a dynamical forcing index, using combinations of q_{225}, vertical wind shear, and the convective available potential energy, with no significant impact on our main results.

The T_g relation to aerosols per preconditioning state. The relation between average T_g and τ_a observed in southern Amazon is shown in Fig. 1. For a very clean atmosphere with τ_a ~0.1, T_g is typically between about −12 and −16 °C. These are equivalent to a natural or background range for T_g, since τ_a corresponds to the average aerosol load in the rainy season in southern Amazon (τ_a ~0.1-0.2). The more moist the upper troposphere, the colder T_g, as the preconditioning effect favors deeper convection[27–29]. At the relative low aerosol content range, with $\tau_a < 0.4$, the intercepts of the T_g *vs.* τ_a relation define the expected maximum average glaciation temperature (at $\tau_a = 0$), ranging from -10.1 ± 0.5 °C (D conditions) to -15.2 ± 0.7 °C (M). In these conditions the aerosol microphysical effect (*cf.* discussion ahead) is represented by the similar slopes found for the T_g *vs.* τ_a relation: about −12.6 °C/unit τ_a, −12.1 °C/unit τ_a, and −13.6 °C/unit τ_a, respectively for D, A, and M conditions. Assuming these three estimates represent the same microphysical phenomenon we calculate the average slope as -12.6 ± 1.7 °C/unit τ_a for $\tau_a < 0.4$.

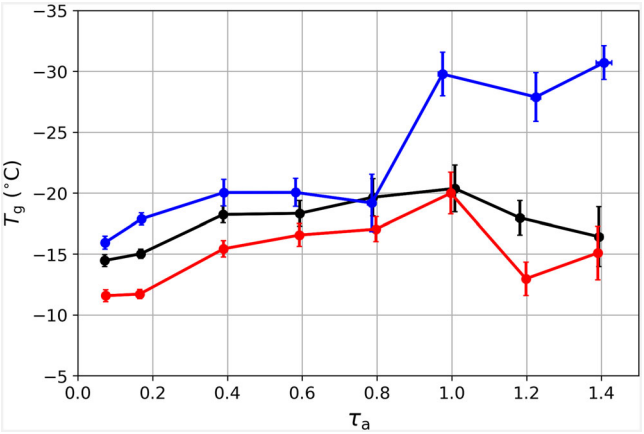

Fig. 1 Glaciation temperature (T_g) in Amazonian convective clouds, from 2000 to 2014, as a function of the columnar aerosol optical depth (τ_a), according to classes of atmospheric preconditioning. Red, black, and blue coloring correspond to lower, mid, and upper tertiles, respectively, in the distribution of q_{225}, a proxy for the convective preconditioning effect. Aerosol data was obtained from daily averages of level 2.0 AERONET[38] measurements at 5 sites in the Amazon Basin. T_g was inferred from GOES satellite imagery acquired in 100 x 100 km boxes around the AERONET sites between 17:00 and 18:00 UTC (13:00-14:00 LT). Error bars correspond to the standard error of the mean. q_{225} was obtained from daily 1° gridded ECMWF Era-Interim reanalysis data[39] at 18:00 UTC.

The slope in the T_g *vs.* τ_a relation is nearly negligible for the $0.4 < \tau_a < 0.8$ section in Fig. 1. T_g is roughly independent of the aerosol signal, and related to the level of preconditioning, with T_g between −15 and −17 °C in D conditions, −18 and −20 °C (A), and −20 and −19 °C in M conditions.

Under heavy pollution ($\tau_a > 0.8$) there are marked differences in T_g patterns. Under D and A preconditioning states, T_g gets warmer with τ_a, i.e., glaciation occurs earlier during the vertical development of convective clouds as the atmospheric smoke loading increases. At the highest τ_a ~1.4 level the glaciation temperature for D and A conditions averages between about −15 and −16 °C, the same range observed for the very clean aerosol range when $\tau_a < 0.4$. To our knowledge, this is the first time this effect is observed. Notice that under M conditions T_g shows a sharp transition for $\tau_a > 0.8$, reaching about −31 °C on average for the most polluted conditions, in general agreement with individual observations of deep convective clouds approaching the limit for homogeneous glaciation[12,13,20]. These results are subsequently discussed.

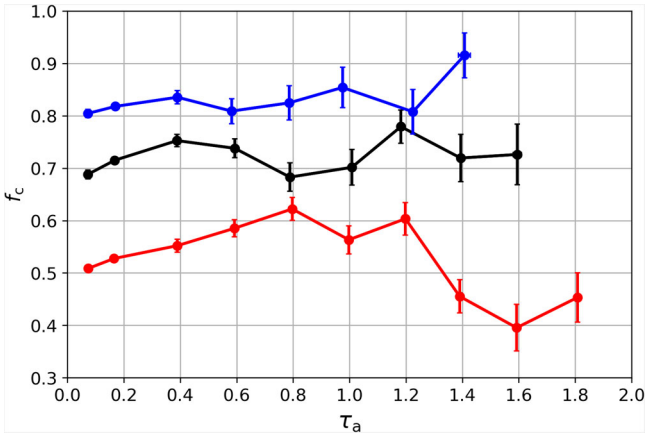

Fig. 2 Cloud fraction (f_c) for convective clouds, from 2000 to 2014, as a function of the columnar aerosol optical depth (τ_a), according to classes of atmospheric preconditioning. Red, black, and blue coloring, error bars and τ_a as in Fig. 1. Cloud fraction was inferred from GOES satellite imagery acquired in 100 x 100 km boxes around the AERONET sites between 17:00 and 18:00 UTC (13:00–14:00 LT).

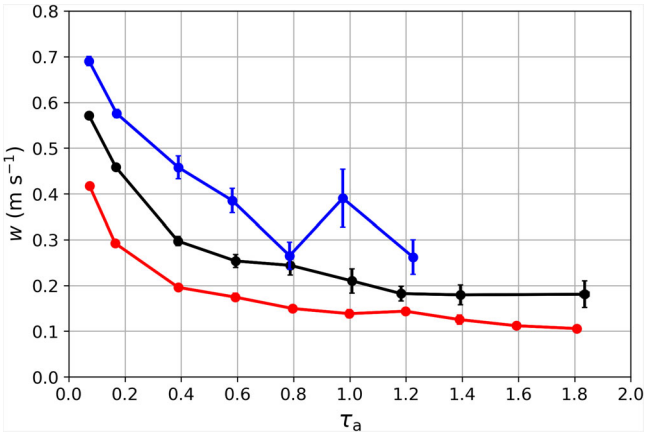

Fig. 3 Updraft velocity at cloud base (w), from 2000 to 2014, as a function of the columnar aerosol optical depth (τ_a), according to classes of atmospheric preconditioning. Red, black, and blue coloring, error bars, and τ_a as in Fig. 1. Updraft velocity at cloud base[41] estimated from ECMWF Era-Interim[39] surface reanalysis data at the five sites used in this study at 18:00 UTC (14:00 LT).

Cloud fraction, cloud base updraft relation to aerosols, and preconditioning. To better understand how T_g may respond to preeminent local drivers of convection in the Amazon, estimates for the cloud fraction (f_c) and the updraft at cloud base (w) were also studied, in relation to aerosols and the preconditioning state. Figure 2 shows that in general, the more moisture present in the upper troposphere, the larger the cloud fraction, which is likely to be an expression of the preconditioning feedback effect itself. Under M conditions f_c ranges from 0.80 to 0.92, showing a slight increase with τ_a. For A conditions f_c oscillates with no clear dependence on the aerosol signal, varying between 0.68 and 0.75. The pattern is clearly nonmonotonic for D conditions, showing an average f_c of 0.51 for a very clean atmosphere (τ_a ~0.1), peaking at 0.62 for τ_a ~0.8, then decreasing to 0.40–0.45 when $1.6 < \tau_a < 1.8$. Note that for the cleaner subset with $\tau_a < 0.40$, f_c increases with τ_a for any preconditioning state, considering the small error bars in this part of Fig. 2.

Reanalysis data were combined with satellite temperature retrievals to derive w, using a validated methodology for Amazonian convective clouds[41]. The method employs the temperature difference observed between the surface and cloud base, assuming a dry adiabatic lapse rate between the two reference levels[41]. Therefore w can also be seen as an instability proxy in the boundary layer. As shown in Fig. 3, the preconditioning effect corresponds to increased w the more moist the upper troposphere, with w averages ranging from a maximum of ~0.69 m s^{-1} under M pristine conditions, to ~0.11 m s^{-1} for D polluted conditions. In general, w decreases nearly monotonically with increasing τ_a. In particular, for D and A conditions, respectively, about 53 and 48% of reduction are observed in the range $\tau_a < 0.40$.

Observations of T_g. Under clean conditions, Amazonian "green ocean" continental clouds can have liquid water content profiles and droplet size distributions that resemble maritime clouds[20]. Hence, we compare our T_g retrievals for Amazon clouds first with pristine conditions over the ocean or land, then in other situations. Reported direct measurements of T_g^* show results[7] such as −10 °C for maritime pristine clouds, or −15 °C for "less maritime" cases (i.e., with smaller droplet sizes). In another work, a T_g^* of about −15 °C in maritime tropical clouds was estimated from in situ measurements showing a rapid decrease in vertical profiles of supercooled water droplet concentrations[15], as most of the precipitate mass freezes at the border between mixed and glaciated phases. These previous results for pristine cases agree with the intercept in Fig. 1 for M conditions, showing a T_g of −15.2 ± 0.7 °C. In particular, Stith et al.[14] performed in situ cloud penetration experiments over one of the Amazonian sites used in this work, and found a T_g^* of −17 °C for measurements in February during the wet season, when the atmosphere in the region is usually pristine, frequently under a moistened preconditioned state with intense convective activity. This matches well Fig. 1 results for $\tau_a < 0.2$, when the average T_g ranges from −16 °C to −18 °C under M conditions. In addition, our results also show how T_g varies in cleaner subset conditions according to the state of atmospheric humidification. We propose here observational constraints for the preconditioning effect in Amazonian clouds at τ_a ~0, in which T_g ranges from −10.1 ± 0.5 °C in D conditions to −15.2 ± 0.7 °C in M conditions. The aerosol microphysical effect manifested itself as an average slope of −12.6 ± 1.7 °C/unit τ_a in this pristine atmosphere limit. These figures can be tested or used in future observational, experimental, or modeling works.

Direct measurements of T_g^* near −38 °C have been reported previously[12,13], which coincide with our coldest individual (i.e., nonaveraged) T_g retrievals under M conditions (*cf.* Supplementary Fig. 2). Note Fig. 1 shows matched-up cloud and aerosol data, resulting in more limited statistics in the final result than in the full database. Measurements of T_g^* ~−38 °C in cumulus clouds have been linked to the availability of abundant cloud condensation nuclei aerosols, which activate smaller droplets that can stay in a supercooled state up to the homogeneous glaciation limit[12,13]. Our results, however, show that when a large amount of aerosols is available, T_g can either approach the −38 °C limit, or remain much lower in the atmosphere, depending on how dynamics primes the atmospheric column for convective activity.

From cloud formation to glaciation. For the cleaner subset, with $\tau_a < 0.4$, cloud droplets will form under an aerosol-limited activation regime[42], when the cloud droplet number concentration is mostly determined by τ_a, and nearly independent of w[42]. Therefore the marked reduction of up to ~53% in w (Fig. 3) should not have a significant impact on the initial droplet number concentration at the cloud base. In general the bigger τ_a, the more

numerous cloud droplets are formed at cloud base[43]. We interpret the linear decrease of T_g with τ_a (Fig. 1), as a consequence of cloud invigoration[2] due to the aerosol microphysical effect, leading to a delay in the occurrence of full glaciation and deeper convective clouds[1,2,44]. The dynamical forcing linked to the preconditioning state also affects T_g, since the more humidified the column, the colder the observed T_g. In these conditions, the radiative extinction effect by aerosols is at its relative minimum. f_c increases by ~4–9% (Fig. 2), indicating a more horizontally spread out cloud field on average, increased shading at the surface, and a more stable boundary layer evidenced by the 34–53% reduction in the magnitude of w (Fig. 3). Nevertheless, since in this regime the cloud droplet population is mostly sensitive to the number of aerosol particles[42], we conclude ultimately the dynamics-microphysics coupling prevails over radiative effects in determining T_g for the cleaner subset.

For the higher pollution subset ($0.4 < \tau_a < 0.8$) the main forcings act simultaneously. As τ_a increases, the average f_c in D conditions grows from about 0.55 to 0.62, a 13% increase (Fig. 2), while in M conditions f_c stays relatively high at about 0.84 within a ~1% variation. This points to a relatively weak importance of the aerosol radiative effect in cloud-free areas, since f_c is either already high or increases with τ_a. Considering the aerosol microphysical effect, as τ_a increases in this polluted conditions range, so does the number concentration of cloud droplets formed initially at cloud base[43]. However, the droplet activation regime[42] undergoes a transition in which w becomes increasingly more important, while its magnitude decreases in general (Fig. 3). These constitute two opposing trends[45] for the number of activated droplets at cloud base, which is critical in determining T_g. M conditions see a reduction of about 42% in the average magnitude of w when $0.4 < \tau_a < 0.8$, while for D conditions the reduction is about 24%; for the average T_g the equivalent changes are about +4.3 and −10% (Fig. 1, M and D conditions, respectively). We cogitate that the sharper relative reduction in w can be the main factor in defining the small increase in T_g for M conditions due to a relative decrease in the concentration of active droplets. In D conditions, the smaller reduction in w and simultaneous increase in τ_a can be possibly associated with an increase in the number of droplets, and hence this could explain the observed reduction in T_g. Therefore we conclude that for these polluted conditions, the dynamics-microphysics coupling probably dominates the observed variations in T_g compared to radiative effects.

Under heavy smoke pollution with $\tau_a > 0.8$, aerosol particles are activated at cloud base in a w-limited activation regime[42], when the number of cloud droplets is mostly sensitive to variations in w and roughly independent of τ_a. Since w is consistently stronger in a moistened column (Fig. 3), denser cloud droplet concentrations occur under M conditions when compared to A or D conditions. Therefore a delay in glaciation[1,2,44] is observed with an average T_g below −30 °C (Fig. 1, M conditions), when a premoistened column sustains the deep convection outset. It is possible secondary ice production processes play a central role in controlling the total concentration of ice particles[46], related to the observed sudden change in T_g. In parallel, as the highest f_c above 0.90 are observed under the same M conditions (Fig. 2), solar radiation extinction by boundary layer aerosols is less prevalent due to more frequent surface shading by clouds, hence the aerosol radiative effect and boundary layer stabilization[22] are relatively less important. For D conditions the smallest observed f_c ~0.40–0.45 results in more frequent mixing between the cloud and external drier air, and also in a relative maximum for aerosol radiative extinction in cloud-free areas. This helps to stabilizing the boundary layer[22,37], and induces the so-called "cloud burning" effect[22,47], a drastic reduction in f_c with increasing τ_a (Fig. 2). In particular, the boundary layer stabilization is evidenced by the smallest w observed under D conditions of ~0.11 m s^{-1} (Fig. 3). In theory[8,30], a parcel ascending through a mixed-phase cloud under drier, subsaturated environmental conditions, with large number concentrations of hydrometeors, and with small in-cloud updraft velocities tends to experience evaporation of liquid droplets and growth of ice particles from water vapor deposition (Wegener–Bergeron–Findeisen process). This is analogous to D conditions in Figs. 1–3 for $\tau_a > 0.8$ (although note Fig. 3 shows the updraft at cloud base, not in-cloud updrafts). Therefore we consider this phenomenon as a possible explanation for the physical process behind the T_g warming with increasing τ_a, with the depletion of liquid droplets and accretion of ice mass at this limit of a driest atmospheric column, more stable boundary layer associated with the smallest w estimates, and heavy pollution. We conclude the relatively warmer T_g of about −13 to −15 °C for D conditions (Fig. 1) is determined by the coupling between the aerosol radiative effect and dynamics set to a drier atmospheric column, unfavorable to deep convection. Conversely, for M conditions the observed T_g below −30 °C is determined by the coupling between moistened preconditioning dynamics and the aerosol microphysical effect.

We showed that T_g in convective clouds in the Amazon is controlled by three main players, with coupled interactions: a) dynamics, represented by the atmospheric preconditioning state; b) aerosol particles, introducing cloud condensation and ice nuclei at cloud base; and c) the radiation field in the boundary layer and surface, which modulates local atmospheric stability and convection initiation. We identify couplings between: i) dynamics and microphysical aerosol effects; and ii) dynamics and radiative aerosol effects. These results provide observational process-informed constraints for deep convection studies in the tropics. They could be used, for instance, to model the depth of the mixed-phase section in convective clouds in a variety of dynamical, microphysical, and radiative scenarios, leading to a more precise description of glaciation in cloud models, with potential developments for climate research[4,5].

Methods

Derivation of T_g. Calibrated radiances measured at three wavelengths (0.63, 3.90, and 11.0 μm) by National Oceanic and Atmospheric Administration's (NOAA) satellites GOES-8, −12, and −13 were analysed in a latitude/longitude box over the Amazon Basin defined between [−02 to −16°N; −49 to −70°E], with daily acquisitions between 17:00 and 18:00 UTC (13:00–14:00 LT), from 2000 to 2014. Radiance in the visible 0.63 μm channel was converted to reflectance ($\rho_{0.63}$), and degraded to 4 km spatial resolution to match the resolution in both infrared channels. Radiance measurements at 11.0 μm were converted to brightness temperature (T_B). The radiance measured at the 3.90 μm channel was converted to reflectance ($\rho_{3.90}$) following the procedure described by Kaufman and Nakajima[21] that accounts for the blackbody radiation emission of clouds in this channel, and its partial absorption in the atmospheric column. Cloudy pixels were defined as having $T_B < +10$ °C and $\rho_{0.63} > 0.15$, at 4 km spatial resolution. In the Amazon, it is possible to have warm clouds forming at temperatures above +10 °C, or having thin cirrus clouds with reflectance below 0.15. Thus, potentially many warm cloud and thin cirrus pixels are not included in the resulting cloudy pixel subset but these thresholds ensure exclusion of shadows, river patches, and vegetated or degraded surface pixels. We tested the influence of adopting different numerical values for the T_B and $\rho_{0.63}$ thresholds, and they had no impact over our main findings. These threshold definitions are therefore suitable for the goals in this study, that focus only on cold top clouds, and do not account for other cloud types.

$\rho_{0.63}$ and $\rho_{3.90}$ were analysed in 100 x 100 km boxes centered around five National Aeronautics and Space Administration (NASA) Aerosol Robotic Network (AERONET[38]) sites: Alta Floresta (AF, −9.87°N, −56.10°E), Abracos Hill (AH, −10.76°N, −62.36°E), Cuiabá (CB, −15.73°N, −56.02°E), Ji Paraná (JP, −10.93°N, −61.85°E), and Rio Branco (RB, −9.96°N, −67.87°E). The ratio R between $\rho_{0.63}$ and $\rho_{3.90}$ for cloudy pixels over each site was analysed according to the thermodynamic phase and season of the year. This was done considering that cloudy pixels with $T_B > 0$ °C corresponded exclusively to liquid phase droplets, while cloudy pixels with $T_B < -38$ °C contained only solid phase particles. Supplementary Fig. 1 shows the histogram of R for each season and thermodynamic phase, for all the ice-only and water-only cloudy pixels used in this study. This corresponds to a total of ~4.6 million pixels, of which ~3.7 million were

observed during the wet season (November to May), and ~0.93 million are from the dry season (June to October). The difference between the number of pixels in each subset reflects the seasonal differences of cloud formation in the Amazon Basin. Supplementary Fig. 1 shows the marked contrast of R values according to the thermodynamic phase of the cloudy pixels, due to differential absorptivity properties of visible and midinfrared wavelengths by water and ice particles[17,48]. Notice that a fully fledged thermodynamic phase detection algorithm is not under discussion here; we rather consider simply that there is a striking distinction in the pattern of the ratio R between liquid-only and solid-only phases. By empirical inspection of Supplementary Fig. 1 the lower limits for the R value of ice particles were defined as 7.62 and 9.63 in the dry and wet seasons, respectively. These R limits effectively allowed the discrimination of ice particles, in the sense that less than 0.40% of water-only pixels in each season showed R values above the ice thresholds. For mixed-phase pixels, the retrieved R is intermediate between the distributions in Supplementary Fig. 1. In this case, the method detects when the prevalent thermodynamic phase matches the ice spectral signature. Dataset retrieved R values showed no significant dependence with τ_a. Because deep convective cells in the Amazon often span several hundreds of kilometers in the horizontal scale (i.e. corresponding to Mesoscale Convective Systems, MCS), the observation of large 3D cloud structures from a geostationary satellite point of view usually spans not only cloud tops but also cloud sides (*cf.* T_g assessment from satellite imagery in SI, and Supplementary Fig. 2). This concept is key to the algorithm since it allows vertically profiling optical properties in a cloud field, including the total glaciation level. The selection of R values above the ice threshold, therefore, covers the total extent of the glaciated phase, from the coldest pixels near the very top of clouds, down to the warmest pixels at temperature T_g, still identified as ice due to their prevalent R spectral signature. The selected pixels were then ranked according to their brightness temperature. The median temperature of the 5% hottest glaciated pixels in 100 km boxes was defined as representing the spatial variability of T_g, thus avoiding high numerical fluctuations associated with extreme values in statistical distributions. This allows accommodating horizontal and vertical variations for the retrieved T_g values over MCS spatial scales, when comparing with τ_a temporal averages[49]. Uncertainty was estimated by circular block bootstrapping[50], by analyzing the monthly T_g time series for each site, using 10,000 replications and a block size of 20 data points (~10 days). Results from all sites were averaged to derive monthly estimates, resulting in uncertainties of 0.6 °C for wet season months (October to April), and 1.1 °C for the dry season (May to September). The different uncertainty levels are mainly due to the more frequent occurrence of clouds in the wet season. Additionally this technique allows identifying the cloud thermodynamic phase. Supplementary Fig. 2 shows an example, where the ice phase (blue) corresponds to pixels colder than T_g, the mixed phase (green) to pixels between 0 °C and T_g, and water clouds (red) correspond to pixels above 0 °C.

This methodology relies only on simple thermodynamic and radiative properties of ice and water in the atmosphere, making it robust for long-term studies, and allows a simple comparison strategy with future works. See additional Methods in SI for the rationale behind the simultaneous analysis of aerosol, atmospheric preconditioning state, and cloud properties, and the use of European Centre for Medium-Range Weather Forecasts (ECMWF) reanalysis datasets in this study.

Data availability

All datasets used in this work are freely available in public repositories. NOAA satellite data can be accessed from the GOES Imager GVAR_IMG product page at https://www.avl.class.noaa.gov/saa/products/search?sub_id=0&datatype_family = GVAR_IMG. NASA aerosol data is available from https://aeronet.gsfc.nasa.gov/cgi-bin/webtool_aod_v3?stage=2&place_code=10&region = South_America&state = Brazil. Reanalysis datasets are available from ECMWF at https://www.ecmwf.int/en/forecasts/dataset/ecmwf-reanalysis-v5.

Code availability

The Python code used for processing the dataset sources used in this study is available from the corresponding author upon request.

Received: 4 January 2021; Accepted: 5 August 2021;
Published online: 19 August 2021

References

1. Rosenfeld, D. et al. Global observations of aerosol-cloud-precipitation-climate interactions: aerosol-cloud-climate interactions. *Rev. Geophys.* **52**, 750–808 (2014).
2. Altaratz, O., Koren, I., Remer, L. A. & Hirsch, E. Review: cloud invigoration by aerosols—Coupling between microphysics and dynamics. *Atmos. Res.* **140–141**, 38–60 (2014).
3. Seinfeld, J. H. et al. Improving our fundamental understanding of the role of aerosol−cloud interactions in the climate system. *Proc. Natl. Acad. Sci.* **113**, 5781–5790 (2016).
4. Lohmann, U. & Neubauer, D. The importance of mixed-phase and ice clouds for climate sensitivity in the global aerosol–climate model ECHAM6-HAM2. *Atmos. Chem. Phys.* **18**, 8807–8828 (2018).
5. Tan, I., Storelvmo, T. & Zelinka, M. D. Observational constraints on mixed-phase clouds imply higher climate sensitivity. *Science.* **352**, 224–227 (2016).
6. Mülmenstädt, J., Sourdeval, O., Delanoë, J. & Quaas, J. Frequency of occurrence of rain from liquid-, mixed-, and ice-phase clouds derived from A-Train satellite retrievals. *Geophys. Res. Lett.* **42**, 6502–6509 (2015).
7. Rosenfeld, D. & Lensky, I. M. Satellite–based insights into precipitation formation processes in continental and maritime convective clouds. *Bull. Am. Meteorol. Soc.* **79**, 2457–2476 (1998).
8. Korolev, A. et al. Mixed-Phase Clouds: Progress and Challenges. *Meteorol. Monogr.* **58**, 5.1–5.50 (2017).
9. Tabazadeh, A., Djikaev, Y. S. & Reiss, H. Surface crystallization of supercooled water in clouds. *Proc. Nat. Acad. Sci.* **99**, 15873–15878 (2002).
10. Li, Z. et al. Long-term impacts of aerosols on the vertical development of clouds and precipitation. *Nat. Geosci.* **4**, 888–894 (2011).
11. Rosenfeld, D., Woodley, W. L., Lerner, A., Kelman, G. & Lindsey, D. T. Satellite detection of severe convective storms by their retrieved vertical profiles of cloud particle effective radius and thermodynamic phase. *J. Geophys. Res.* **113**, D04208 (2008).
12. Rosenfeld, D. & Woodley, W. L. Deep convective clouds with sustained supercooled liquid water down to -37.5 °C. *Nature.* **405**, 440–442 (2000).
13. Rosenfeld, D., Woodley, W. L., Krauss, T. W. & Makitov, V. Aircraft microphysical documentation from cloud base to anvils of hailstorm feeder clouds in Argentina. *J. Appl. Meteorol. Climatol.* **45**, 1261–1281 (2006).
14. Stith, J. L., Haggerty, J. A., Heymsfield, A. & Grainger, C. A. Microphysical characteristics of tropical updrafts in clean conditions. *J. Appl. Meteorol.* **43**, 779–794 (2004).
15. Lawson, R. P., Woods, S. & Morrison, H. The microphysics of ice and precipitation development in tropical cumulus clouds. *J. Atmos. Sci.* **72**, 2429–2445 (2015).
16. Yuan, T., Martins, J. V., Li, Z. & Remer, L. A. Estimating glaciation temperature of deep convective clouds with remote sensing data. *Geophys. Res. Lett.* **37**, L08808 (2010).
17. Martins, J. V. et al. Remote sensing the vertical profile of cloud droplet effective radius, thermodynamic phase, and temperature. *Atmos. Chem. Phys.* **11**, 9485–9501 (2011).
18. Rosenfeld, D. et al. Glaciation temperatures of convective clouds ingesting desert dust, air pollution and smoke from forest fires. *Geophys. Res. Lett.* **38**, L21804 (2011).
19. Ten Hoeve, J. E., Remer, L. A., Correia, A. L. & Jacobson, M. Z. Recent shift from forest to savanna burning in the Amazon Basin observed by satellite. *Environ. Res. Lett.* **7**, 024020 (2012).
20. Andreae, M. O. Smoking rain clouds over the Amazon. *Sci.* **303**, 1337–1342 (2004).
21. Kaufman, Y. J. & Nakajima, T. Effect of Amazon smoke on cloud microphysics and albedo analysis from satellite imagery. *J. Appl. Meteorol.* **32**, 729–744 (1993).
22. Koren, I. Measurement of the effect of Amazon smoke on inhibition of cloud formation. *Sci.* **303**, 1342–1345 (2004).
23. Schiro, K. A., Neelin, J. D., Adams, D. K. & Lintner, B. R. Deep convection and column water vapor over tropical land versus tropical ocean: a comparison between the Amazon and the tropical western pacific. *J. Atmos. Sci.* **73**, 4043–4063 (2016).
24. Malhi, Y., Pegoraro, E., Nobre, A. D., Pereira, M. G. P. & Grace, J. Energy and water dynamics of a central Amazonian rain forest. *J. Geophys. Res.* **107**, 8061 (2002).
25. Zhuang, Y., Fu, R., Marengo, J. A. & Wang, H. Seasonal variation of shallow-to-deep convection transition and its link to the environmental conditions over the Central Amazon. *J. Geophys. Res.* **122**, 2649–2666 (2017).
26. Silva Dias, M. A. F. et al. Cloud and rain processes in a biosphere-atmosphere interaction context in the Amazon Region. *J. Geophys. Res.* **107**, 8072 (2002).
27. Brown, R. G. & Zhang, C. Variability of midtropospheric moisture and its effect on cloud-top height distribution during TOGA COARE. *J. Atmos. Sci.* **54**, 15 (1997).
28. Waite, M. L. & Khouider, B. The deepening of tropical convection by congestus preconditioning. *J. Atmos. Sci.* **67**, 2601–2615 (2010).
29. Holloway, C. E. & Neelin, J. D. Moisture vertical structure, column water vapor, and tropical deep convection. *J. Atmos. Sci.* **66**, 1665–1683 (2009).
30. Korolev, A. Limitations of the Wegener–Bergeron–Findeisen mechanism in the evolution of mixed-phase clouds. *J. Atmos. Sci.* **64**, 3372–3375 (2007).
31. Petersen, W. A. & Rutledge, S. A. Regional variability in tropical convection: observations from TRMM. *Journal of Climate* **14**, 3566–3586 (2001).

32. Blyth, A. M. Entrainment in Cumulus Clouds. *J. Appl. Meteorol.* **32**, 626–641 (1993).
33. Chen, Q. et al. How do changes in warm-phase microphysics affect deep convective clouds? *Atmos. Chem. Phys.* **17**, 9585–9598 (2017).
34. Koren, I., Dagan, G. & Altaratz, O. From aerosol-limited to invigoration of warm convective clouds. *Science.* **344**, 1143–1146 (2014).
35. McCluskey, C. S. et al. Characteristics of atmospheric ice nucleating particles associated with biomass burning in the US: Prescribed burns and wildfires. *J. Geophys. Res. Atmos.* **119**, 10458–10470 (2014).
36. Lohmann, U. A glaciation indirect aerosol effect caused by soot aerosols. *Geophys. Res. Lett.* **29**, 1052 (2002).
37. Hansen, J., Sato, M. & Ruedy, R. Radiative forcing and climate response. *J. Geophys. Res.* **102**, 6831–6864 (1997).
38. Holben, B. N. et al. AERONET—a federated instrument network and data archive for aerosol characterization. *Remote Sens. Environ.* **66**, 1–16 (1998).
39. Berrisford, P. et al. Atmospheric conservation properties in ERA-Interim. *Q. J. R. Meteorol. Soc.* **137**, 1381–1399 (2011).
40. Balsamo, G. et al. ERA-Interim/Land: a global land surface reanalysis data set. *Hydrol. Earth Sys. Sci.* **19**, 389–407 (2015).
41. Zheng, Y. & Rosenfeld, D. Linear relation between convective cloud base height and updrafts and application to satellite retrievals. *Geophys. Res. Lett.* **42**, 6485–6491 (2015).
42. Reutter, P. et al. Aerosol- and updraft-limited regimes of cloud droplet formation: influence of particle number, size and hygroscopicity on the activation of cloud condensation nuclei (CCN). *Atmos. Chem. Phys.* **9**, 7067–7080 (2009).
43. Andreae, M. O. Correlation between cloud condensation nuclei concentration and aerosol optical thickness in remote and polluted regions. *Atmos. Chem. Phys.* **9**, 543–556 (2009).
44. Tao, W.-K., Chen, J.-P., Li, Z., Wang, C. & Zhang, C. Impact of aerosols on convective clouds and precipitation. *Rev. Geophys.* **50**, RG2001 (2012).
45. Stevens, B. & Feingold, G. Untangling aerosol effects on clouds and precipitation in a buffered system. *Nature.* **461**, 607–613 (2009).
46. Ladino, L. A. et al. On the role of ice-nucleating aerosol in the formation of ice particles in tropical mesoscale convective systems. *Geophys. Res. Lett.* **44**, 1574–1582 (2017).
47. Ackerman, A. S. et al. Reduction of tropical cloudiness by soot. *Science.* **288**, 1042–1047 (2000).
48. Riedi, J. et al. Cloud thermodynamic phase inferred from merged POLDER and MODIS data. *Atmos. Chem. Phys.* **10**, 11851–11865 (2010).
49. Hoelzemann, J. J. et al. Regional representativity of AERONET observation sites during the biomass burning season in South America determined by correlation studies with MODIS Aerosol Optical Depth. *J. Geophys. Res.* **114**, D13301 (2009).
50. Marchand, R., Beagley, N., Thompson, S. E., Ackerman, T. P. & Schultz, D. M. A bootstrap technique for testing the relationship between local-scale radar observations of cloud occurrence and large-scale atmospheric fields. *J. Atmos. Sci.* **63**, 2813–2830 (2006).

Acknowledgements

We thank NOAA GOES, NASA AERONET, and ECMWF ERA-Interim teams for the datasets used in this study. A.L.C. and E.T.S. thank the Brazilian National Council for Scientific and Technological Development (CNPq) for research grants 472303/2012-0 and 421870/2018-4. A.L.C. thanks the São Paulo Research Foundation (FAPESP) for research grant SeReNA 2010/15959-3.

Author contributions

A.L.C. initiated the study, analysed, interpreted the data, and wrote the paper. E.T.S. participated in the analysis and interpretation of data, and contributed to the writing. M.A.F.S.D. and I.K. participated in science discussions and analyses, and contributed to the writing.

Competing interests

The authors declare no competing interests.

Additional information

Supplementary information The online version contains supplementary material available at https://doi.org/10.1038/s43247-021-00250-3.

Correspondence and requests for materials should be addressed to A.L.C.

Peer review information *Communications Earth & Environment* thanks the anonymous reviewers for their contribution to the peer review of this work. Primary Handling Editor: Heike Langenberg. Peer reviewer reports are available.

Reprints and permission information is available at http://www.nature.com/reprints

Publisher's note Springer Nature remains neutral with regard to jurisdictional claims in published maps and institutional affiliations.